1. Extended Data

Figure #	Figure title One sentence only	Filename This should be the name the file is saved as when it is uploaded to our system. Please include the file extension. i.e.: *Smith_ED_Fig1.jpg*	Figure Legend If you are citing a reference for the first time in these legends, please include all new references in the main text Methods References section, and carry on the numbering from the main References section of the paper. If your paper does not have a Methods section, include all new references at the end of the main Reference list.
Extended Data Fig. 1	**Nuclear pores across different imaging modalities.**	**Extended Data Fig. 1.pdf**	(a) A schematic of the Nup96 complex, taken from Thevathasan et al. (2019). 3D MINFLUX rendered data presented for comparison from Gwosch et al. (2020) (colormap removed for comparison). Note the uneven distribution in *xz*, compared with the EM model (Von Appen et al. (2015) and dSTORM data in Thevathasan et al. (2019) Fig. 2h. (b) Membrane protein gp210 from amphibian oocytes imaged with dSTORM (Alexa Fluor 647). The 8-fold symmetry and circular structure of NPCs are generally seen. The diameter of gp210 is 164 ± 7 nm. Image adapted from Loeschberger et al (2012). (c) Nup96 endogenously labeled with SNAP-tag-Alexa Fluor 647 in U2OS cell lines. 8- and 7-component pores are more commonly observed. The effective labeling efficiency for SNAP-Alexa Fluor 647 was ~60%. Image adapted from Thevathasan et al. (2019). (d) MINFLUX imaging of U2OS cell expressing Nup96–SNAP labelled with Alexa Fluor 647. In these cases (selected from Gwosch et al. (2020) Fig. 2a), 6- and 7- component nuclear pores are more prominent throughout the FOV, raising a question about detection efficiency. Localizations were rendered with a Gaussian kernel, σ = 2 nm, to visualize the 4 individual copies of Nup96 per NPC subunit (1–5 sub-clusters per subunit apparent here). In multi-color MINFLUX

			imaging, the localizations in a subunit appear as a larger, undefined cluster **(h)**. Cell line and labeling strategy as in Thevathasan et al. (2019). Image adapted from Gwosch et al. (2020). (e) Average images of gp210 (outer ring, *N* = 426) and WGA (central channel, *N* = 621) of the NPC. The outer ring (gp210) has an average diameter of ~164 nm. The diameter of the inner ring (WGA) is ~40 nm. Image adapted from Loeschberger et al (2012). Scale bar: 100 nm. (f) dSTORM images of WGA labeled with ATTO 520 (green) and gp210 labeled with Alexa Fluor 647 (pink) in amphibian oocytes. Both the outer ring and inner channel are visible (Loeschberger et al. 2012). (g) Two-color SMLM image of Nup96-SNAP-Alexa Fluor 647 (red) and WGA-CF680 (cyan) in U2OS cell lines. The outer ring is clearly visible and the inner ring is also visible in most cases. Image adapted from Thevathasan et al. (2019). (h) Two-color MINFLUX imaging of U2OS cell expressing Nup96–SNAP labeled with Alexa Fluor 647 and WGA conjugated to CF680. The subunits of the outer ring, which each have 4 copies of Nup96, now appear as single clusters (comparing with **c**). The inner ring (WGA) also appears as undefined aggregations of the signal. Image adapted from Gwosch et al. (2020).
Extended Data Fig. 2	**Visualization of the inner ring of nuclear pores (wheat germ agglutinin (WGA)**	**Extended Data Fig. 2.pdf**	Scatter plots showing localizations from 10 segmented WGA complexes from the 3D, 2-color MINFLUX dataset. The segmented complexes did not contain rings of localizations as found by Thevathasan et al. (2019) and Loeschberger et al (2012). Scale bar: 20 nm.

Extended Data Fig. 3	**MINFLUX localization filtering**	**Extended Data Fig. 3.pdf**	Scatter plots for 2D, 1-color (a); 3D, 1-color (b); 3D, 2-color (c); and 2D, live (d) unfiltered and filtered MINFLUX datasets. The raw MINFLUX data comes in a tabular format, with a Boolean flag indicating that localization was assigned as either a background event or a true molecular event (Gwosch et al. (2020), Extended Data Table 2). For the final data, we give the density of true localizations over the FOV defined by the total molecular emission events before filtering. Scale bar: 500 nm (a), 200 nm (b), 500 nm (c), 50 nm (d) in the published data column.
Extended Data Fig. 4	**NPC tilt and *z*-distances**	**Extended Data Fig. 4.pdf**	A 2D projection model of the two-layer NPC (**a**) requires its axis to be tilted (θ) by 36° for an inter-layer distance (ILD) of 50 nm between localizations to result in an average measurement in the *z*-direction ($\langle ILD_z \rangle$) of 40.5 nm. Considering *z*-measurements only from the center point of the lower layer to all points on the upper layer, ILD_z has a range ($Range(ILD_z)_{center}$) of 63 nm, when the diameter (D) of the projected NPC is 107 nm. Including *z*-measurements from all points in the lower layer to all points on the upper layer doubles the total range of ILD_z to 125 nm, which is large compared with $\langle ILD_z \rangle$. Therefore if localizations with ILD of 50 nm were measured to have $\langle ILD_z \rangle$ of 40.5 nm, we would expect the NPCs to be tilted to ~36° and also expect *z*-measurements between the layers to have a broad spread,

			before considering additional spread owing to a distribution of NPC tilt angles. Distributions of **Δ*z*** between localizations in a 3D NPC model (**b**) show a similar pattern. The NPC model used localizations with a two-layer, 8-fold radially symmetric structure, with an inter-layer distance of 50 nm and diameter of 107 nm. At each value of θ (tilt of the model axis from the *z*-direction), the model was also rotated about its axis by angles φ from 0 to 44° in 1° increments. **Δ*z*** values were found between all localizations at each rotation angle φ and aggregated over φ to result in an averaged distribution at each tilt angle θ. In agreement with the 2D model (**a**), the inter-layer distance peak moved to shorter distances for higher tilt angles θ, approaching 40 nm between θ = 30° and θ = 40°. The inter-layer distance peak was still close to 50 nm at θ = 10°. In further agreement with **a**, and as may be intuitively expected, broadening of the **Δ*z*** distribution with increasing θ significantly reduced the contrast of the inter-layer distance peak for $\theta \geq 20°$. Therefore, it is highly unlikely that the high-contrast peak at 40.5 nm (**Fig. 2g,h**) of the experimental **Δ*z*** distribution of the data of Gwosch et al. (2020) Fig. 3f would be generated by two layers of localizations with an inter-layer distance of 50 nm, tilted at 30–40°. Rather, we support the statement

			of Gwosch et al. that the layers of the NPCs in Gwosch et al. (2020) were typically parallel to the focal plane. We also support this statement as a reasonable approximation in a 3D scatter plot of the localizations (**c**, Extended Data **Video 1**) of Gwosch et al. (2020) Fig. 3f. In this plot, NPC layers, when discernible, appear generally to be roughly parallel to a fitted curve representing nuclear envelope curvature (quadratic in *x* and *y*, fitted to the localization coordinates). The mean inclination of this surface at the localization coordinates is 5° (maximum: 9°). At θ = 5°, an ILD of 50 nm would result in $\langle ILD_z \rangle$ of 49.8 nm (**a**), or a fractional difference of 0.4% between ILD and $\langle ILD_z \rangle$. A narrow distribution of local NPC tilts with a peak at this angle may be expected (e.g. s.d. 12° in Heydarian et al., *Nat Commun* 12, 2847 (2021)). Our result in **Fig. 2g,h**, therefore, reflects the inter-layer distance of the acquired localizations, not a projection of a two-layer structure at large tilt angles. Furthermore, a similar 3D plot and fit (**d**, Extended Data **Video 2**) of the Nup96 localizations of Gwosch et al. (2020) Fig. 5c shows a similar (but denser) distribution of NPCs. In this case, the mean fitted nuclear envelope inclination was 2° (maximum: 5°),

			and we also expect NPCs to have a similar distribution of local tilt angles centered on this angle (Heydarian et al., 2021). In this case, we found an inter-layer distance of 50.9 nm (**Fig. 2i,j**), which is in fact greater than the calculation of Gwosch et al. at ~46 nm, despite the similar NPC tilts between the two datasets. From these considerations (**a**–**d**), the difference between our inter-layer distance results of 40.5 nm and 50.9 nm for the two datasets are not explained by a difference in NPC tilts.
Extended Data Fig. 5	**dSTORM localization density from Thevathasan et al. (2019)**	**Extended Data Fig. 5.pdf**	From publicly available data (https://www.ebi.ac.uk/biostudies/BioImages/studies/S-BIAD8), localization densities were calculated over the nuclear regions shown. Compared to 2D, 1-color MINFLUX data (Fig 3) which has an average localization density of 435 μm^{-2}, 2D, 1-color dSTORM has a ~6x greater average localization density of 2739 μm^{-2}. Scale bar: 3 μm in (1) and 1 μm in (2), (3), (4).
Extended Data Table 1	**Corrected Akaike Information Criterion values (AICc) and relative likelihoods for different symmetric models fitted to the Δxy**	**Extended Data Table 1.pdf**	AICc and relative likelihoods for each model to be the best model were calculated as for Nup107 distributions in Curd et al. (2021).

	distributions of Fig. 2		
Extended Data Table 2	**MINFLUX raw dataset (localisation positions and filtering data) as provided by the authors (Gwosch et al. 2020)**	**Extended Data Table 2.pdf**	x_est_absolute[double]: Absolute estimated molecule position in um. y_est_absolute [double]: Absolute estimated molecule position in um. N [double]: Number of photons used for localization. p0 [double]: Ratio of photons collected for central STC position. r_relative [double]: Relative distance of molecule position with respect to the central STC position in um. filter [logical] (1-color data only): Boolean flag result of event filters. True: localization is valid (molecular emission event) False: localization is invalid (background event). moleculeID [double]: ID of molecular emission event.

2. Supplementary Information:

A. Flat Files

Item	Present?	Filename This should be the name the file is saved as when it is uploaded to our system, and should include the file extension. The extension must be .pdf	A brief, numerical description of file conter i.e.: *Supplementary Figures 1-4, Supplementary Disc Supplementary Tables 1-4.*
Supplementary Information	No		

Reporting Summary	Yes	NMETH-MA45218Creportingsumm.pdf
Peer Review Information	No	*OFFICE USE ONLY*

B. Additional Supplementary Files

Type	Number If there are multiple files of the same type this should be the numerical indicator. i.e. "1" for Video 1, "2" for Video 2, etc.	Filename This should be the name the file is saved as when it is uploaded to our system, and should include the file extension. i.e.: *Smith_ Supplementary_Video_1.mov*	Legend or Descriptive Caption Describe the contents of the file
Supplementary Video	1	**Extended Data Video 1.avi**	-
Supplementary Video	2	**Extended Data Video 2.avi**	-

3. Source Data

Parent Figure or Table	Filename This should be the name the file is saved as when it is uploaded to our system, and should include the file extension. i.e.: *Smith_SourceData_Fig1.xls,* or *Smith_ Unmodified_Gels_Fig1.pdf*	Data description i.e.: Unprocessed Western Blots and/or gels, Statistical Source Data etc.
Source Data Fig. 1	Prakash_SourceData_Fig1.csv	Statistical Source Data

Assessment of 3D MINFLUX data for quantitative structural biology in cells

Kirti Prakash[1, 2, 4] **and Alistair P. Curd**[3, 4]

[1]National Physical Laboratory, TW11 0LW Teddington, UK; [2]Integrated Pathology Unit, Centre for Molecular Pathology, The Royal Marsden Trust and Institute of Cancer Research, SM2 5NG Sutton, UK; [3]School of Molecular and Cellular Biology, University of Leeds, Leeds LS2 9JT, UK; [4]Correspondence: kirtiprakash2.71@gmail.com; a.curd@leeds.ac.uk

Arising from: Nature Methods https://www.nature.com/articles/s41592-019-0688-0 (2020)

In 2017, Balzarotti et al.[1] introduced MINFLUX to localize individual fluorophores in single-molecule localization microscopy by probing the emitter with a doughnut-shaped excitation beam[1]. The authors attained a precision ≈1 nm and resolved loci on DNA origami placed 6 nm apart. In 2020, Gwosch et al.[2] extended the method to fixed and living biological cells, and into 3D and two colors, claiming resolutions in the range of 1–3 nm for subcellular structures[2]. Using nuclear pore complexes (NPCs) as an example, the authors measured localization precisions of 1–3 nm and asserted (1) that MINFLUX can clearly resolve the eightfold symmetry of Nup96 in single nuclear pores; (2) Nup96 is distributed along a ring of 107 nm in diameter; and (3) that 3D MINFLUX can resolve the parallel cyto and nucleoplasmic layers of Nup96 in single pore complexes, ≈50 nm apart in the axial (*z*) direction. However, we were not convinced by the evidence given for these claims and have therefore reanalyzed the datasets provided by the authors.

We agree with their main localization precision results, but in our reanalysis we found (1) that the eightfold symmetry of NPCs is rarely visible at a single nuclear pore level and was not clearly determined in structure-based modelling of the localization datasets; (2) that the mean or best-fit Nup96 ring diameter varies between datasets and the spread of diameters in each dataset is broader than that found by dSTORM[3]; and (3) the average *z*-distance between cyto- and nucleoplasmic layers of Nup96 localizations was 40.5 nm instead of ≈50 nm, in the dataset on which this claim was based. Furthermore, in 2-color imaging, the inner ring found in similar dSTORM experiments at 40-nm diameter[3,4] was not resolved as a ring by MINFLUX. We therefore conclude that while these MINFLUX datasets demonstrate high 3D precision in localizing molecules, they do not appear to demonstrate the accuracy of previously published state-of-the-art dSTORM imaging of NPCs[3].

Per-pore analysis. We first assessed the MINFLUX datasets by estimating the diameter of segmented Nup96 complexes (Fig 1a–c). Qualitatively, Nup96 appeared less well sampled, comparing the number and uniformity of clusters per NPC with previous dSTORM data[3], and there was a large range of numbers of localizations per NPC (Fig 1e). Using circle fits as described by Thevathasan et al.[3], we found the diameter distributions in the 2D, 3D 1-color and 3D 2-color datasets (Gwosch et al.[2] Fig. 2a, 3f, 5c) to be 107 ± 10 nm, 108 ± 7 nm and 111 ± 5 nm (mean ± s.d., $N = 20$), respectively. The Nup96 ring diameter in a dataset was therefore not simply 107 nm, as stated by Gwosch et al.[2] and referenced by them in dSTORM and electron microscopy data[3,5], and it had a previously unreported spread. Our estimates for the spread of diameters (Fig 1d) for MINFLUX data were larger than that for dSTORM data (radius 53.7 ± 2.1 nm, so diameter 107.4 ± 4.2 nm, $N = 2{,}536$)[3], and the 3D 2-color MINFLUX diameters were statistically different from dSTORM results and the stated 107 nm (see Methods). Gwosch et al.[6] later presented the observation of nanometer scale variability as a strength of MINFLUX, but did not explain why this variability was greater than in previous dSTORM data. We are therefore not convinced that MINFLUX outperforms dSTORM for this type of measurement and scale of a biological feature.

For 2-color, 3D MINFLUX imaging of the NPC, Gwosch et al.[2] show labelled wheat germ

agglutinin (WGA-CF680) residing inside the Nup96 octamer both laterally and axially. However, while dSTORM has previously resolved an inner ring of the NPC with WGA-CF680 and measured its diameter at 41 ± 7 nm with WGA-AF647[3,4], such structure was neither apparent in the MINFLUX data (Extended Data Fig. 1) nor discussed. Even after segmentation and closer inspection of WGA distributions, we could not visually discern a ring-like structure (Extended Data Fig. 2). Therefore, we conclude that for this particular sample, MINFLUX, unlike dSTORM, failed to resolve a □40 nm ring structure.

FOV ensemble analysis. We next analyzed the distribution of MINFLUX localizations in a field of view (FOV) using PERPL[7], a structure-based modelling technique designed for incomplete data, as is often the case for single-molecule localization microscopy (SMLM)[7] (Fig. 2). Specifically, we calculated the relative position distribution (RPD) of Nup96 localizations and used its components in the lateral (*xy*) (Fig. 2a–f) and axial (*z*) directions (Fig. 2g–j).

For structures in *xy*, a model RPD that performed well for dSTORM localizations of Nup107[7] was fitted to the histogram of the experimental distances between MINFLUX localizations (Fig. 2a–f). Localization precision estimates (σ_{xy}) were 0.98 ± 0.02 nm, 3.20 ± 0.05 nm and 3.31 ± 0.08 nm (fitted value ± 1 s.d. uncertainty) for the 2D, 3D 1-color and 3D 2-color datasets, respectively, of Gwosch et al.[2], which broadly agree with the published analysis. Secondary peaks may indicate consistent substructure within clusters in the 2D dataset down to a distance of 7 nm (Fig. 2a, not modeled). However, this detail is lost in the 3D and 2-color datasets (Fig. 2c,e). If σ_{xy} is in the range of 1–3 nm, we question whether the resolution is possible at 1–3 nm, as is claimed. For instance, Gaussian full width at half maximum (FWHM) ≈ 2.355σ, so σ_{xy} of 1–3 nm implies FWHM of 2.4–7.1 nm for a single molecule, and we would not expect to resolve molecules closer than this clearly.

Estimates of the Nup96 ring diameters varied from 104 to 109 nm and orders of symmetry from 7- to 9-fold, for the different datasets (Fig. 2a–f, Supplementary Table 1). The best fits do not follow the experimental distance distribution as closely as for Nup107 dSTORM data[7], which may be due to the effect of intra-cluster substructure (Fig. 2a,b), a more variable arrangement of Nup96, or a smaller number of NPCs and localizations in the FOV. In particular, filtering out a larger fraction of localizations (Extended Data Fig. 3) appears to have caused the background to deviate from linear (Fig. 2a,b) to a more complex distribution (Fig. 2c–f). These analyses are not consistent with the claim that MINFLUX obtains a diameter of exactly 107 nm and 8-fold symmetry, as reported by Gwosch et al.[2], who did not perform any structural analysis in *xy*. Such conclusive results may be difficult to obtain from these datasets, with small numbers of NPCs (*N* □ 20–30, including incomplete complexes), and larger datasets would be useful to establish them.

In the axial (*z*) direction, using PERPL (Fig. 2g–j), we estimated localization precision (σ_z) at 2.28 ± 0.05 nm and 3.08 ± 0.06 nm for the 3D, 1-color and 2-color datasets of Gwosch et al.[2], demonstrating the high localization precision in *z*, and implying that best possible resolution in *z* ≈ 5–7 nm (FWHM). For the 3D 1-color dataset of Gwosch et al.[2] Fig. 3f, we found the distance between the Nup96 layers to be 40.5 ± 0.2 nm (Fig. 2g,h), and not □50 nm, as claimed by Gwosch et al. (no quantitative analysis provided)[2] and previously obtained in dSTORM[3]. In contrast, in the 2-color dataset of Gwosch et al.[2] Fig. 5c, we estimated the inter-layer distance at 50.89 ± 0.08 nm (Fig. 2i,j), close to the expected □50 nm (and estimated at □46 nm by Gwosch

et al.). We also verified that the different results from the data of Gwosch et al.[2] Fig. 3f and Fig. 5c were not explainable by a difference in nuclear envelope inclination or local NPC tilt (Extended Data Fig. 4, Supplementary Videos 1, 2); we agree with Gwosch et al.[2], who noted that the NPC layers were typically parallel to the focal plane. Gwosch et al.[6] have later explained this difference by disagreeing both with their original publication on this point[2] and with modeling and 3D visualization of the data (Extended Data Fig. 4, Supplementary Videos 1, 2). Thus, we were not convinced that MINFLUX provides accurate quantitative measures in the axial direction.

Localization probability, live-cell results. We reproduced the published images of Gwosch et al.[2] and noted that localization densities are low (~450–1200 μm^{-2}, Extended Data Fig. 3a–c), compared with representative regions in dSTORM on the same sample type with the same labelling method (~2600–3450 μm^{-2}, Extended Data Fig. 5, Thevathasan et al.[3]). Fewer data points, meaning reduced signal, are therefore available for structural resolution. We also note that a lower probability of target molecules being localized results in increased noise in structural information, from false negatives in localizing real features in the structure. These effects on the signal-to-noise ratio may be the reason for structures appearing less clear and for differences in quantitative results and their uncertainties, despite very high localization precisions, as noted. Additionally, this may explain the higher accuracy of the inter-layer distance for the data with higher localization density (Fig. 2h,j, Extended Data Fig. 3b,c).

The lowest localization density was obtained for live-cell data, as is often the case in SMLM. With N = 2 NPCs and 38 localizations (Extended Data Fig. 3d, Gwosch et al.[2] Fig. 2f), there was too little data available to assess the claim of resolution at 1–3 nm in living cells. Circular fits found diameters of 102 nm and 104 nm (Figure 1f, ideal result 107 nm). We are therefore unable to quantitatively assess σ_{xy}, resolution and reliability in this case, since we could not use PERPL analysis on only two instances of the NPC with missing data.

Furthermore, Gwosch et al.[2] did not calculate localization precision in the live sample. In a fixed sample, they measured σ_{xy} □2 nm for the same label, Nup96-mMaple (Gwosch et al.[2] Supplementary Fig. 7), which gives a possible resolution limit (≈ FWHM) of □5 nm in that case. However, precision and resolution are generally degraded when moving from fixed to live specimens, so we do not expect nanometer (1–3 nm) resolution in the case of live MINFLUX imaging, based on these datasets.

Discussion. From our reanalysis of the data reported by Gwosch et al.[2], we were unable to confirm that MINFLUX delivers 3D multicolor nanometer resolution (1–3 nm) for structures in fixed and living cells, at the current stage of the technology. In fact, it generated less precise and reliable results than established SMLM methods and appeared unable to resolve a 40-nm ring structure, despite using the same sample and comparable labeling methods to those in previous dSTORM data[2,3].

After event filtering, 3D Nup96-AF647 localization precision in fixed samples is impressive at σ = 1–3 nm. However, we advise against interpreting localization precision (σ) as resolution, which is intuitively understood as the minimum distance separating two nearby features at which they can be distinguished. Resolution is worse than 2σ at a lower limit and is affected by other factors such as localization density, or the probability of localizing target molecules. We note that methods that increase localization precision may also reduce localization probability (including event filtering) and thus worsen resolution. This merits further exploration when resolving

structural information is the goal, in this and other SMLM methods. We suggest assessing resolution, detection efficiency and exploration of event filtering algorithms on blind samples, to demonstrate the potential of this new technology. For an initial discussion of these issues, see Prakash[8].

We fully expect MINFLUX methods to continue to improve, as they have done in the powerful iterative and 3D developments already reported[2]. However, we recommend that experimentalists also perform initial testing of the resolution, detection efficiency and exploration of event filtering algorithms on potential samples, to the extent this is possible, before choosing MINFLUX over other SMLM techniques.

Acknowledgments

We would like to thank Lothar Schermelleh, Johannes Hohlbein, Michelle Peckham and Peter Knight for helpful discussions. A.P.C. gratefully acknowledges funding by the UK Biotechnology and Biological Sciences Research Council (BB/S015787/1) and the Wellcome Institutional Strategic Support Fund (University of Leeds).

Author Contributions:

K.P. conceived the project. K.P. and A.P.C. designed the project, performed data analysis, interpreted results and wrote the manuscript.

Competing Interests: The authors declare that they have no known competing financial interests or personal relationships that could influence the work reported in this paper.

References

1. Balzarotti, F., Eilers, Y., Gwosch, K. C., Gynnå, A. H., Westphal, V., Stefani, F. D., Elf, J., and Hell, S. W. (2017). Nanometer resolution imaging and tracking of fluorescent molecules with minimal photon fluxes. *Science*, 355(6325):606–612.
2. Gwosch, K. C., Pape, J. K., Balzarotti, F., Hoess, P., Ellenberg, J., Ries, J., and Hell, S. W. (2020). Minflux nanoscopy delivers 3d multicolor nanometer resolution in cells. *Nature methods*, 17(2):217–224.
3. Thevathasan, J. V., Kahnwald, M., Ciesli ´ nski, K., Hoess, P., Peneti, S. K., Reitberger, M., Heid, D., Kasuba, K. C., Hoerner, S. J., Li, Y., et al. (2019). Nuclear pores as versatile reference standards for quantitative superresolution microscopy. *Nature methods*, 16(10):1045–1053.
4. Löschberger, A., van de Linde, S., Dabauvalle, M.-C., Rieger, B., Heilemann, M., Krohne, G., and Sauer, M. (2012). Super-resolution imaging visualizes the eightfold symmetry of gp210 proteins around the nuclear pore complex and resolves the central channel with nanometer resolution. *J Cell Sci*, 125(3):570–575.
5. Von Appen, Alexander, et al. "In situ structural analysis of the human nuclear pore complex." *Nature* 526.7571 (2015): 140-143.
6. Gwosch, Klaus, et al. "Assessment of 3D MINFLUX data for quantitative structural biology in cells revisited." *bioRxiv* (2022), doi: 10.1101/2022.05.13.491065.
7. Curd, A. P., Leng, J., Hughes, R. E., Cleasby, A. J., Rogers, B., Trinh, C. H., Baird, M. A., Takagi, Y., Tiede, C., Sieben, C., et al. (2021). Nanoscale pattern extraction from

relative positions of sparse 3d localizations. *Nano letters*, 21(3):1213–1220.
8. Prakash, Kirti. "At the molecular resolution with MINFLUX?." *Philosophical Transactions of the Royal Society A* 380.2220 (2022): 20200145.

Fig. 1. Visualisation of individual nuclear pores. Scatter plots showing localizations from single Nup96 complexes for 2D, 1-color (a); 3D, 1-color (b); 3D, 2-color (c); and 2D, live (f) MINFLUX datasets. Distributions of the fitted diameter (d) and the number of localizations (e) among the NPCs. Box plots show mean ± s.d., also stated. We segmented N = 20 NPCs for each dataset (a–e) and show those with minimum/maximum diameter and minimum/maximum number of localizations for the outer rings of Nup96 (a–c). Two Nup96 complexes were visible in the live data (f).

Fig 2: Relative position distributions and model analysis. Histograms of *xy*- and *z*-distances (Δxy, Δz) between localizations, bin-width 1 nm. Counts scaled to a mean of 1 to optimize the performance of the fitting algorithm. Δxy distribution for the Nup96 localizations of Gwosch et al.[2] Fig. 2a (a), 3f (c) and 5c (e) and fits to them (b, d, f,) of nuclear porin models from 6- to 10-fold symmetry, including repeated single-molecule localizations (Δxy), intra- and inter-cluster distances within an NPC, and background~inter-pore distances[7]. Symmetry, nuclear pore diameter (D) and σ_{xy} for the model selected by AICc[7] in each experiment (b, d, f). Indications of resolved intra-cluster substructure in a (*). Δz distribution for the data in Gwosch et al.[2] Fig. 3f (g) and 5c (i) and fit with a model including two layers of localizations and repeated single-molecule localizations (σ_z) (h, j).

Methods:

In per-pore analysis (Fig. 1), we used the MATLAB function *circlefit* (https://uk.mathworks.com/matlabcentral/fileexchange/5557-circle-fit) to fit a circle to a set of (x, y) points.

Statistical analysis of 3D 2-color MINFLUX diameters of Nup96 rings, compared with reference results[3,5] used the *stats* module within the Python library *scipy* 1.3[9]. The distribution of the 20 MINFLUX diameters was tested for normality[10,11] and accepted (*stats.normaltest*, p = 0.13). The more precise mean ± standard deviation of the 3D 2-color diameters is 110.7 ± 5.2 nm (N = 20). The mean MINFLUX diameter was statistically different from 107 nm (quoted from electron microscopy data by Gwosch et al.[2]) (1-sample t-test, two-tailed: t = 3.159, p = 0.005), using the 20 measured diameter values. The mean MINFLUX diameter was also significantly different

from the previous dSTORM result on Nup96 ring diameters with the same sample and comparable labelling methods[2,3] (107.4 ± 4.2 nm, N = 2,536)[3] (Welch's unequal variances t-test, two-tailed: t = 2.888, p = 0.009), using the sample means and standard deviations.

FOV ensemble analysis (Fig. 2, Extended Data Fig. 4) used PERPL[7] 0.12m (https://bitbucket.org/apcurd/perpl-python3/commits/tag/0.12m). The *xy*-model includes Gaussian clusters arranged symmetrically around a ring, repeated localizations of a single molecule (with s.d. spread σ_{xy}), and a linearly increasing background term. The most likely order of symmetry is selected using corrected Akaike information criteria, which are calculated from the residuals of the model fits (SupplementaryTable 1). The *z*-model includes two layers of localizations, each with a Gaussian distribution in *z*, a term for localization precision (σ_z) for repeated localizations of a single molecule, and constant background.

Nup96 structural model selection (Fig. 2, Supplementary Table 1) used the corrected Akaike's Information Criterion (AICc)[12], as in Curd et al.[7]. Briefly, lower AICc values among compared models indicate quantitatively that less information from the real data distribution is lost when the fitted models are used to approximate the real data. Lower AICc thus results in higher relative likelihoods among compared models. The AICc is a relative value among models being compared, not an absolute value, and cannot be compared across different datasets (e.g. results for 2D, 1-color can be compared with each other, but not with results for 3D, 1-color). As a guide, if AICc differs by 6 between models, one is 20 times more likely to be the best model than the other (ratio: $\exp\left(-\frac{1}{2}\Delta AICc\right)$)[12].

Localization density (Extended Data Figs. 3,5) was calculated as the number of MINFLUX events labeled as true localizations, divided by the area of the FOV as defined by the ranges in x and y of all localizations before filtering.

Data availability: The original MINFLUX data[2] was made available by Stefan Hell. All the re-analyzed data has been deposited to Zenodo at https://doi.org/10.5281/zenodo.5214631.

Code availability: Plots for Fig. 2 and Extended Data Fig. 4 were generated using PERPL[7] 0.12m, available at https://bitbucket.org/apcurd/perpl-python3/commits/tag/0.12m.

Methods-only references

9. Virtanen, P., Gommers, R., Oliphant, T. E., Haberland, M., Reddy, T., Cournapeau, D., ... & Van Mulbregt, P. (2020). SciPy 1.0: fundamental algorithms for scientific computing in Python. *Nature methods*, *17*(3), 261–272.
10. D'Agostino, R. B. (1971). An omnibus test of normality for moderate and large size samples. *Biometrika*, *58*(2), 341–348.
11. D'Agostino, R., & Pearson, E. S. (1973). Tests for departure from normality. Empirical results for the distributions of b_2 and $\sqrt{b_1}$. *Biometrika*, *60*(3), 613–622.
12. Burnham, K. P., & Anderson, D. R. (1998). Practical use of the information-theoretic approach. In *Model selection and inference* (pp. 75–117). Springer, New York, NY.

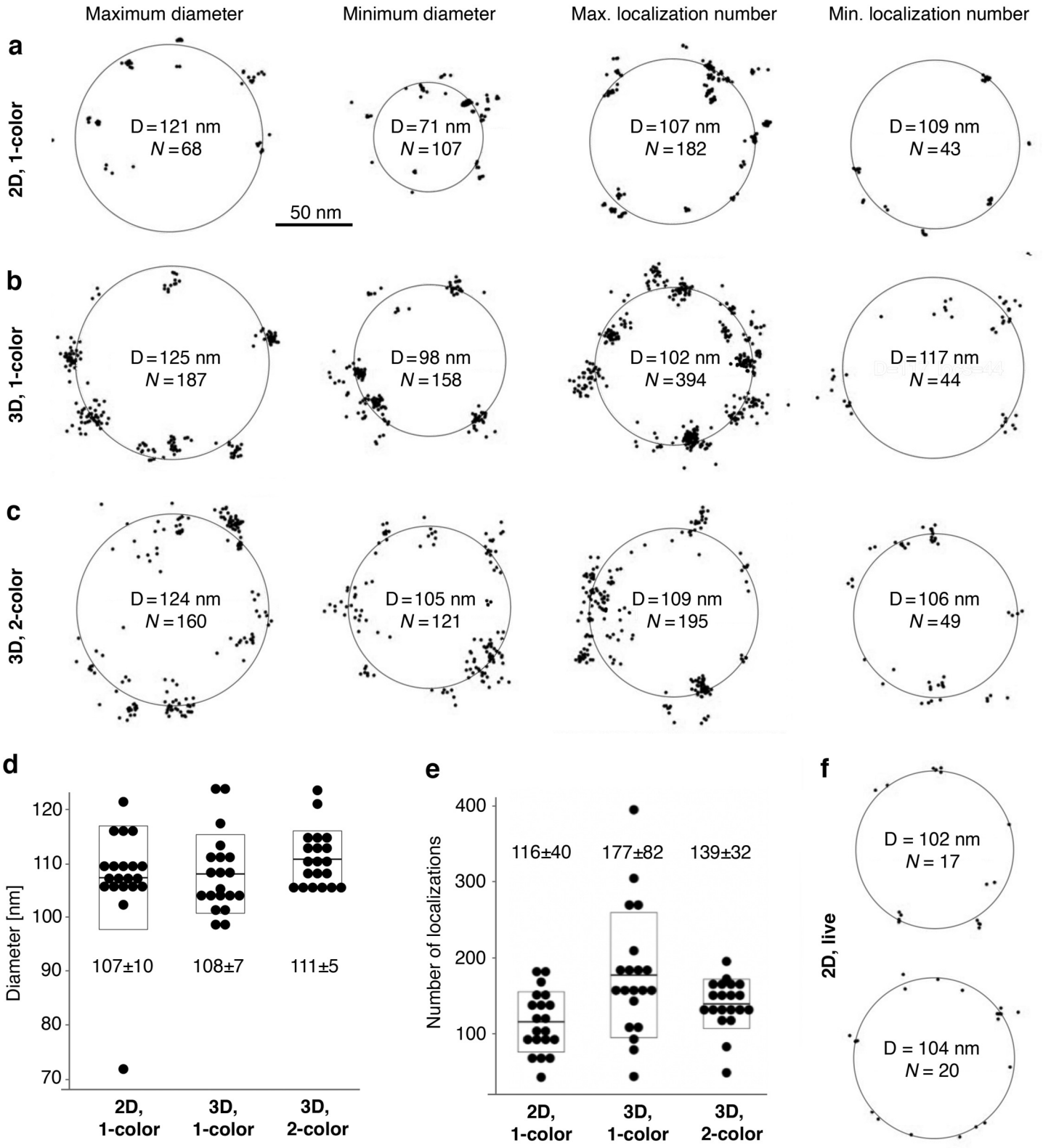
Maximum diameter
Minimum diameter
Max. localization number
Min. localization number
a
2D, 1-color
D = 121 nm
N = 68
D = 71 nm
N = 107
D = 107 nm
N = 182
D = 109 nm
N = 43
50 nm
b
3D, 1-color
D = 125 nm
N = 187
D = 98 nm
N = 158
D = 102 nm
N = 394
D = 117 nm
N = 44
c
3D, 2-color
D = 124 nm
N = 160
D = 105 nm
N = 121
D = 109 nm
N = 195
D = 106 nm
N = 49
d
Diameter [nm]
120
110
100
90
80
70
107±10
108±7
111±5
2D, 1-color
3D, 1-color
3D, 2-color
e
Number of localizations
400
300
200
100
116±40
177±82
139±32
2D, 1-color
3D, 1-color
3D, 2-color
f
2D, live
D = 102 nm
N = 17
D = 104 nm
N = 20

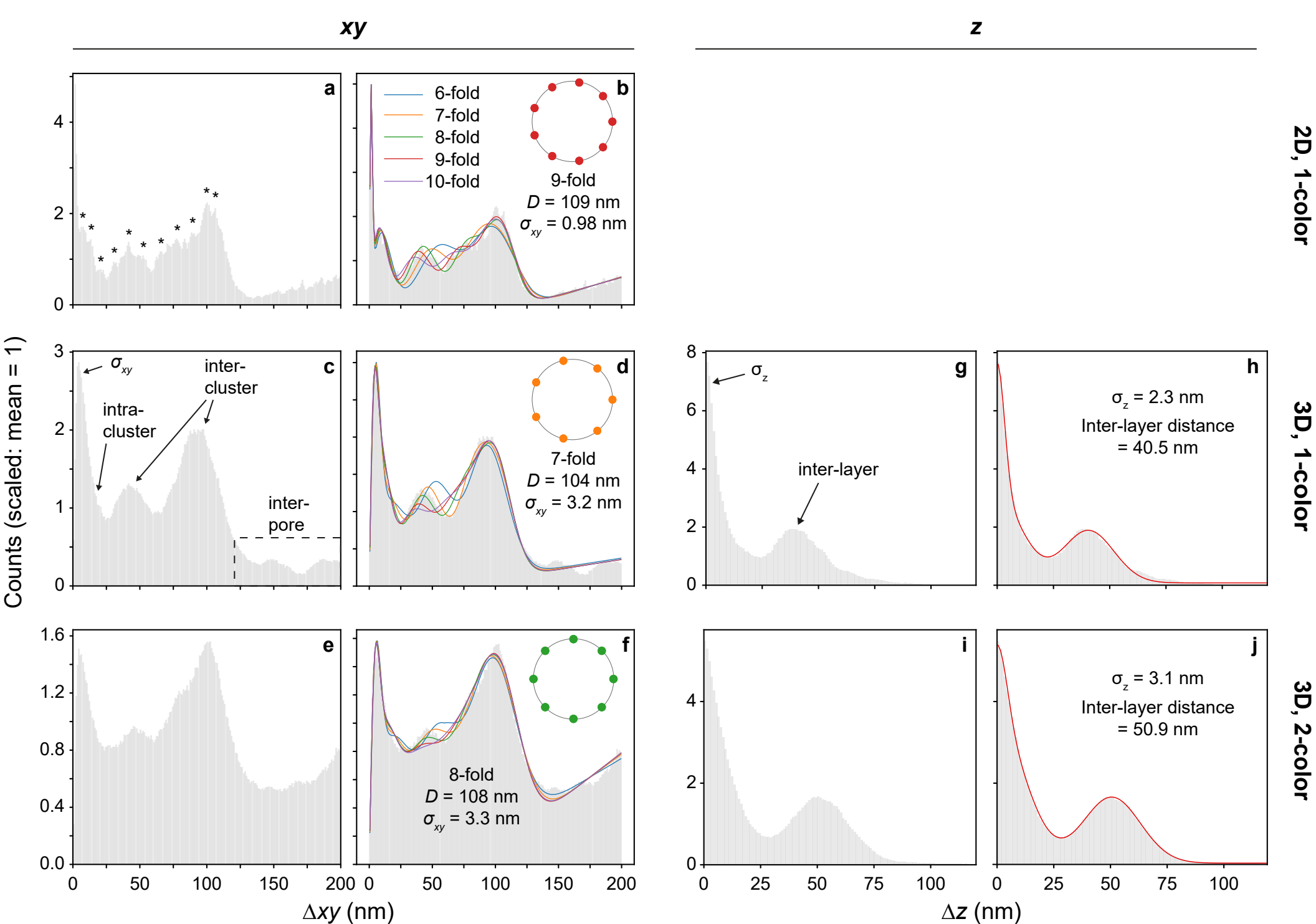
xy
z
2D, 1-color
3D, 1-color
3D, 2-color
Counts (scaled: mean = 1)
a
b
6-fold
7-fold
8-fold
9-fold
10-fold
9-fold
D = 109 nm
σxy = 0.98 nm
c
σxy
intra-cluster
inter-cluster
inter-pore
d
7-fold
D = 104 nm
σxy = 3.2 nm
g
σz
inter-layer
h
σz = 2.3 nm
Inter-layer distance = 40.5 nm
e
f
8-fold
D = 108 nm
σxy = 3.3 nm
i
j
σz = 3.1 nm
Inter-layer distance = 50.9 nm
Δxy (nm)
Δz (nm)

Löschberger et al. 2011
Löschberger et al. 2011
Thevathasan et al. 2019
Gwosch et al. 2020
Combined
Inner ring
Outer ring
e
f
g
h
Thevathasan et al. 2019
Löschberger et al. 2011
Thevathasan et al. 2019
Gwosch et al. 2020
3D MINFLUX (rendered)
Side view
Top view
50 nm
42 nm
107 nm
12 nm
7
8
7
a
b
c
d

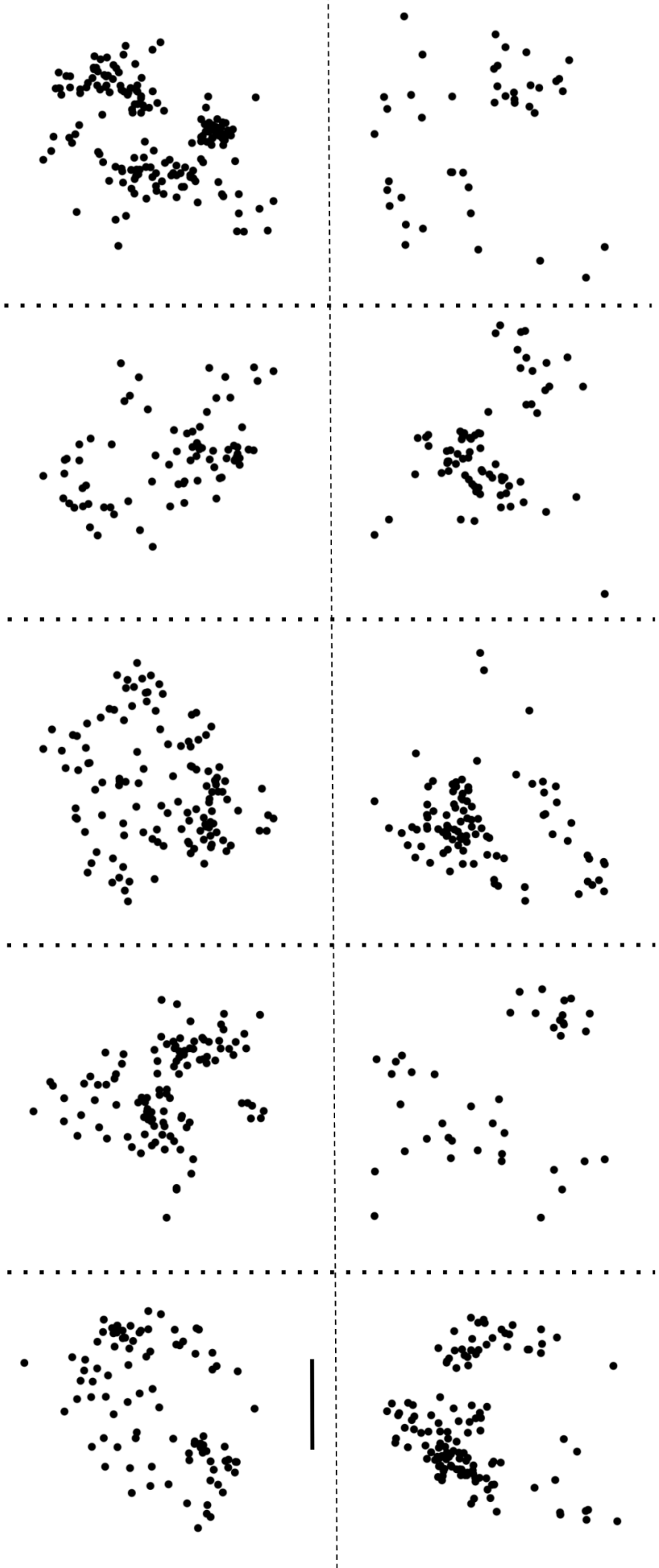

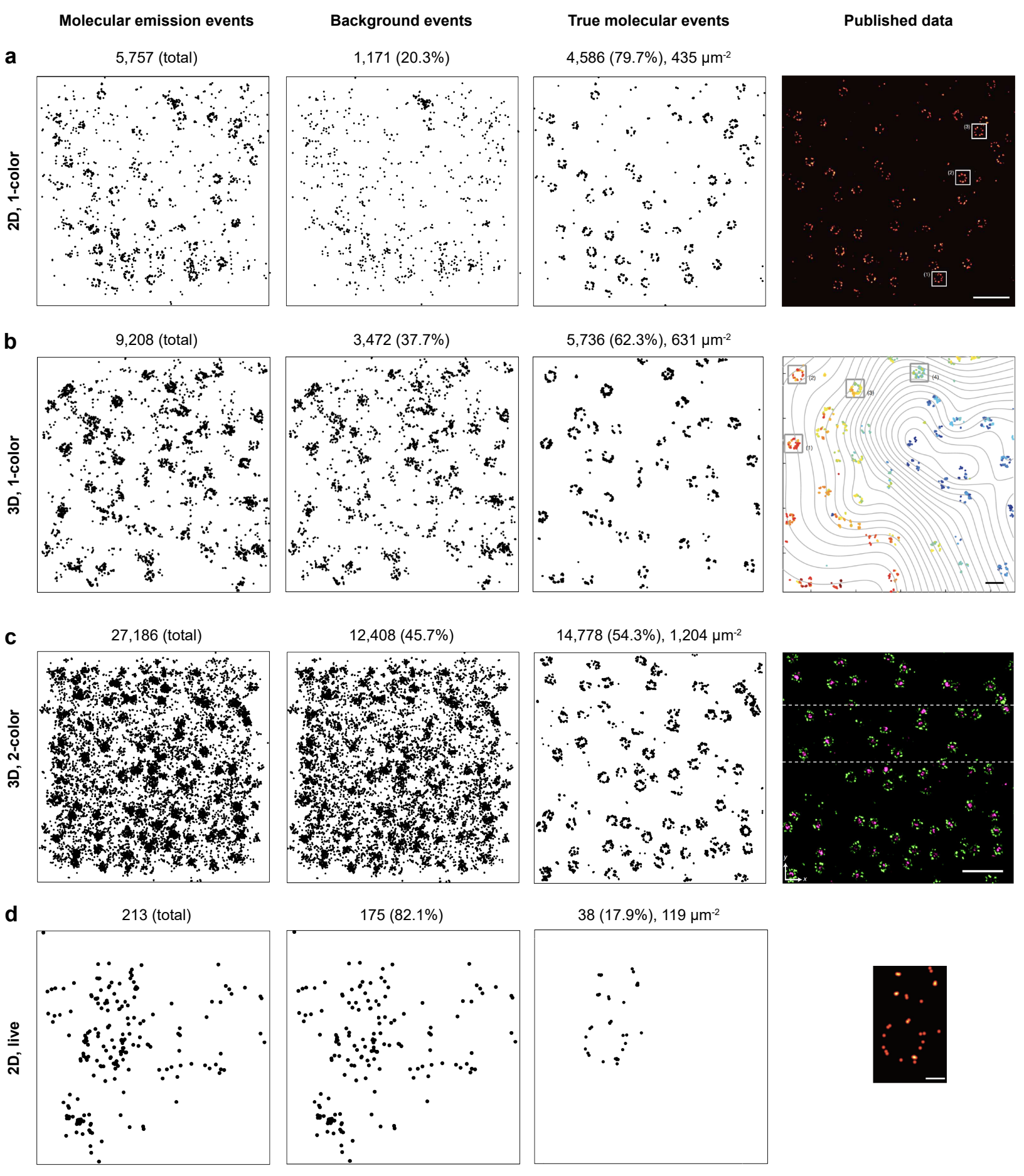
Molecular emission events
Background events
True molecular events
Published data
a
5,757 (total)
1,171 (20.3%)
4,586 (79.7%), 435 μm-2
2D, 1-color
b
9,208 (total)
3,472 (37.7%)
5,736 (62.3%), 631 μm-2
3D, 1-color
c
27,186 (total)
12,408 (45.7%)
14,778 (54.3%), 1,204 μm-2
3D, 2-color
d
213 (total)
175 (82.1%)
38 (17.9%), 119 μm-2
2D, live

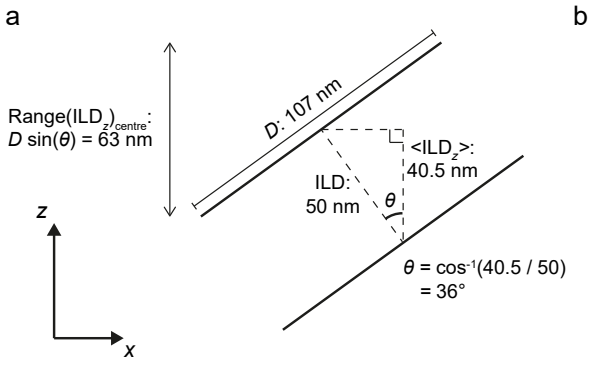

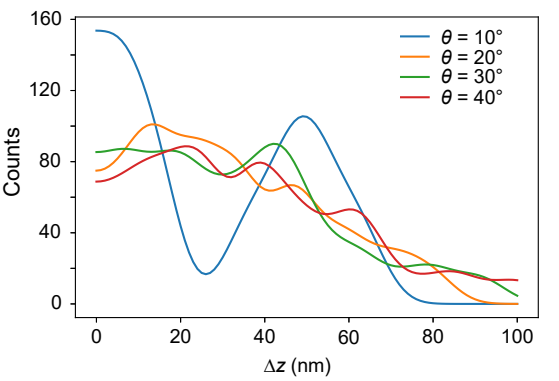

XZ 2D approximation

3D simulation, including rotations about NPC axis

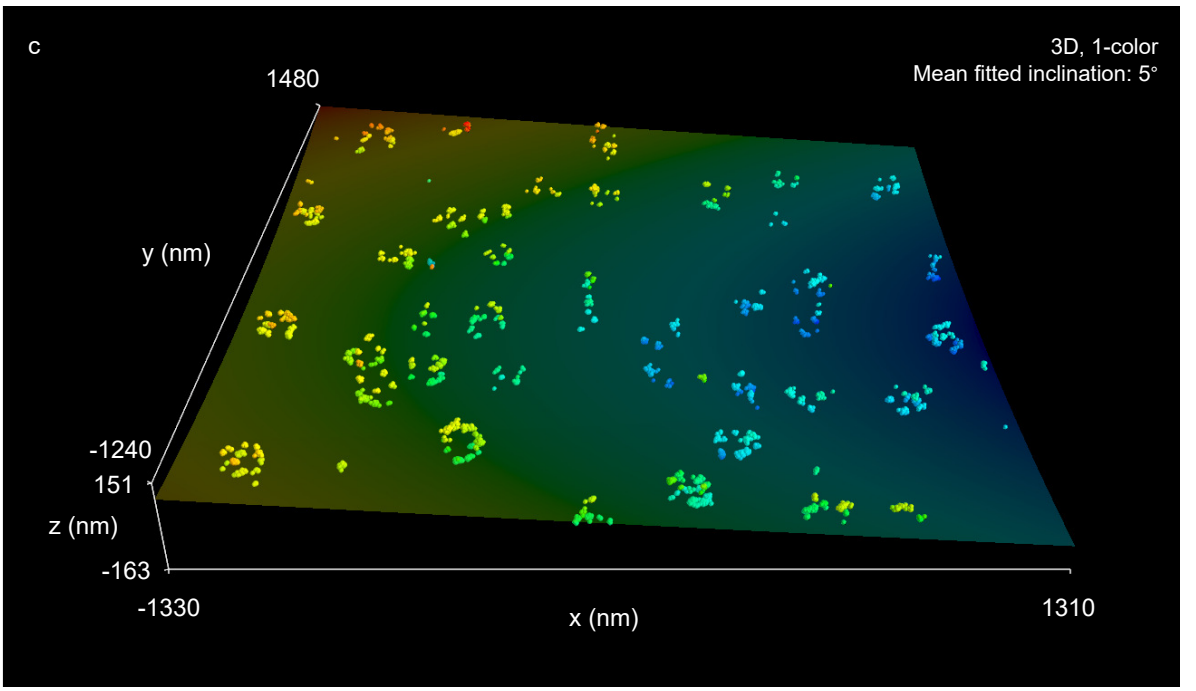

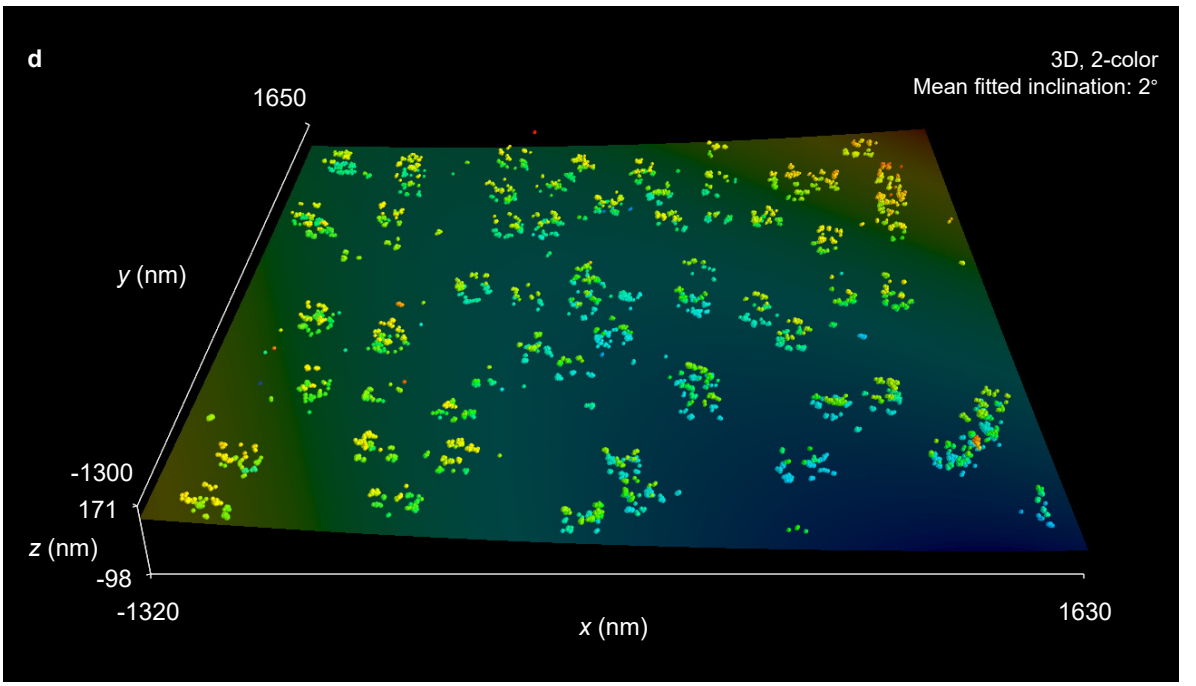

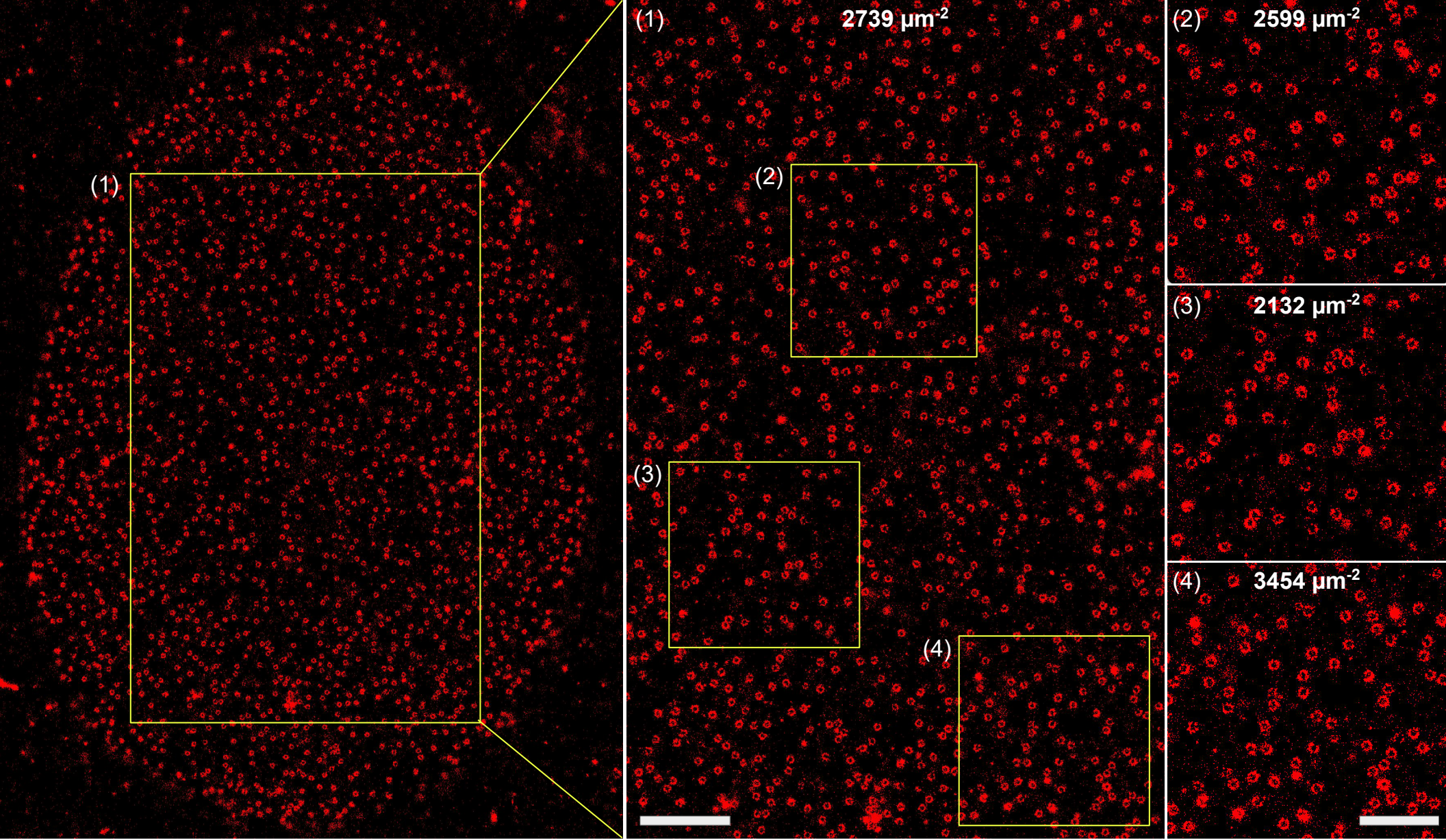
(1)
(1) 2739 µm-2
(2)
(3)
(4)
(2) 2599 µm-2
(3) 2132 µm-2
(4) 3454 µm-2

	2D, 1-color		3D, 1-color		3D, 2-color	
	AICc	Relative likelihood	AICc	Relative likelihood	AICc	Relative likelihood
6-fold	−564.92	<0.01	−768.43	<0.01	−1114.98	<0.01
7-fold	−648.93	<0.01	−988.03	1	−1149.43	<0.01
8-fold	−816.15	<0.01	−945.01	<0.01	−1171.03	1
9-fold	−877.36	1	−876.87	<0.01	−1154.44	<0.01
10-fold	−801.00	<0.01	−859.74	<0.01	−1138.56	<0.01

	x_est_absolute	y_est_absolute	N [double]	p0 [double]	r_relative	Filter	molecularID
1	571.23	1246.22	3401	0.07	0	1	1
2	569.37	1245.37	2003	0.07	0.01	1	2
3	570.61	1243.29	1999	0.06	0.01	1	2
4	570.77	1244.45	2000	0.07	0.01	1	2
5	571.49	1244.61	3905	0.07	0.01	1	2
6	571.61	1245.34	2912	0.06	0.01	1	2
7	569.73	1243.96	3570	0.05	0	1	3
8	-569.06	-200.72	2001	0.26	0.02	0	4
9	-567.14	-199.52	2001	0.25	0.03	0	4
10	-568.3	-200.28	2188	0.25	0.03	0	4